

Journal of Materials Chemistry A

Accepted Manuscript



This is an *Accepted Manuscript*, which has been through the Royal Society of Chemistry peer review process and has been accepted for publication.

Accepted Manuscripts are published online shortly after acceptance, before technical editing, formatting and proof reading. Using this free service, authors can make their results available to the community, in citable form, before we publish the edited article. We will replace this *Accepted Manuscript* with the edited and formatted *Advance Article* as soon as it is available.

You can find more information about *Accepted Manuscripts* in the [Information for Authors](#).

Please note that technical editing may introduce minor changes to the text and/or graphics, which may alter content. The journal's standard [Terms & Conditions](#) and the [Ethical guidelines](#) still apply. In no event shall the Royal Society of Chemistry be held responsible for any errors or omissions in this *Accepted Manuscript* or any consequences arising from the use of any information it contains.

Graphene-based Electrochemical Filter for Water Purification

Cite this: DOI: 10.1039/x0xx00000x

Yanbiao Liu,^{a,b} Juen Hon Dustin Lee,^a Qing Xia,^a Ying Ma,^b Yang Yu,^a Lin Yue Lanry Yung,^c Jianping Xie,^c Choon Nam Ong,^b Chad D. Vecitis^d and Zhi Zhou^{a,b,s,*}

Received 00th January 2014,
Accepted 00th January 2014

DOI: 10.1039/x0xx00000x

www.rsc.org/

A novel graphene-based electrochemical filter with carbon nanotubes as conductive binders was developed for water purification. Ferrocyanide ($\text{Fe}(\text{CN})_6^{4-}$) was used as a model compound to study electron transfer mechanisms in the electrochemical filter. A 70%:30% ratio of graphene:carbon nanotube was optimal for electrochemical oxidation of $\text{Fe}(\text{CN})_6^{4-}$, and electrooxidation rates increased linearly with increasing concentration of influent $\text{Fe}(\text{CN})_6^{4-}$. The results of chronoamperometry and normal pulse voltammetry indicated that mass transfer increased up to 15-fold in the electrochemical filter as compared to a batch electrooxidation system. Finally, the efficiency of graphene-based filters for electrooxidation of organic pollutants was evaluated with three selected organic compounds. The oxidation rates increased with increasing anode potential and reached maximum removal rates of $0.010 \text{ mol hr}^{-1} \text{ m}^{-2}$ (88% removal), $0.064 \text{ mol hr}^{-1} \text{ m}^{-2}$ (93% removal), and $0.014 \text{ mol hr}^{-1} \text{ m}^{-2}$ (87% removal) at an applied anode potential of 0.8 V (vs. Ag/AgCl) for tetracycline, phenol, and oxalate, respectively. Overall, the results exemplified the advantages of contaminant removal using a graphene electrode in a flow-through system and demonstrated the potential of using graphene-based electrochemical filters for water purification.

Introduction

Development of cost-effective water treatment techniques is critical to tackle global water quality challenges. Membrane processes, such as microfiltration, ultrafiltration, nanofiltration, and reverse osmosis are promising among state-of-the-art water treatment technologies.¹ An emerging inorganic membrane material is carbon nanotube (CNT) with combined advantageous properties of stability, flexibility, chemical resistivity, and large specific surface area.²⁻⁶ Furthermore, CNT conductivity allows for effective electrochemical filtration for sorption and oxidation of aqueous organic pollutants such as azo dyes and phenol.^{7,8} Hinds and co-workers have previously explored the use of aligned CNT-polymer composite membrane for filtration applications.⁹ However, the CNT-based membranes are not ready for full-scale practical applications due to the properties of CNT macrostructures¹⁰ and other technical difficulties.¹¹

Graphene is another elemental carbon nanomaterial and could be used as membranes for water treatment. Graphene is a 2D one-atom-thick layer of graphite,¹² and has attracted significant attention due to its high electrical and thermal conductivity, mechanical strength,¹³ optical and chemical properties,¹⁴ solution processability,¹⁵ and specific surface area up to $2630 \text{ m}^2 \text{ g}^{-1}$.¹⁶ The toxicity of graphene was reported lower than that of CNT, because graphene is synthesized by the exfoliation of highly pure graphite and avoids residual metal impurities in CNT metal-catalysis-driven growth process that

usually result in toxicity.¹⁷ Therefore, graphene has been widely used in flexible transparent electrodes,¹⁸ solar cells,¹⁹ energy storage devices,²⁰ and electronics and optoelectronics.^{21, 22} Graphene nanoplatelets (GNP) can form highly ordered membranes or films by facile filtration-assisted assembly,²³ chemical vapour deposition,²⁴ electrochemical deposition,²⁵ and layer-by-layer methods.²⁶ The rich surface chemistry of the 2D graphene favors fine tuning the interfacing properties with various supporting materials. More important, cost-effective mass production of GNP has recently made considerable progress.²⁷⁻³⁰ GNP can significantly enhance the reactivity of extant elemental carbon-based materials, such as graphite, activated carbon, fullerene, and carbon nanotubes,³¹ during redox reactions,^{32, 33} photocatalysis,³⁴ and electrocatalysis.³⁵⁻³⁷

Although graphene has many advantageous properties, the current research on its environmental applications has mainly focused on material fabrication^{23, 38} and chemical sorption.¹¹ For example, an ultra-thin (22-53 nm) reduced graphene oxide nanofiltration membrane was prepared via vacuum filtration and showed high sorption of organic dyes (>99%, via π - π interactions) and moderate retention of ion salts (>20%, via *Donnan* exclusion).¹¹ However, the short breakthrough time due to limited sorption sites on graphene membranes has limited its application. For example, our results indicated that breakthrough occurred in <30 min for 0.1 mmol L^{-1} tetracycline and 0.53 mmol L^{-1} phenol (Fig. S1), suggesting that physical adsorption to graphene is not sustainable for water purification.

The objective of this study was to develop a novel graphene-based electrochemical filter to utilize both the high specific surface area and high conductivity of graphene to physically adsorb and electrochemically oxidize chemical contaminants. The filter was optimized with ferrocyanide ($\text{Fe}(\text{CN})_6^{4-}$) as a model target molecule,^{39, 40} which is non-sorptive and undergoes a single electron transfer and therefore oxidation can be easily and quantitatively monitored by spectrophotometry and chronoamperometry.^{41, 42} The effects of influent concentration, anode potential, and anode material composition on $\text{Fe}(\text{CN})_6^{4-}$ electrooxidation were examined. The electrochemical filter was then compared with a conventional batch system to evaluate the effect of internal electrode convection. Finally, the efficacy and efficiency of organic pollutant electrooxidation with the graphene-based filter were evaluated using three selected organic compounds: tetracycline (a common antibiotic released from wastewater treatment plant), phenol (a common organic compound in industrial wastewater and presents at superfund sites), and oxalate (a recalcitrant small organic).

Experimental section

Chemicals and materials. Sodium sulfate (Na_2SO_4 , $\geq 99.0\%$), potassium hexacyanoferrate (II) trihydrate ($\text{K}_4\text{Fe}(\text{CN})_6 \cdot 3\text{H}_2\text{O}$, 98.5-102.0%), potassium phthalate monobasic ($\text{C}_8\text{H}_5\text{KO}_4$, $\geq 99.5\%$), sodium carbonate (Na_2CO_3 , $\geq 99.8\%$), tetracycline ($\text{C}_{22}\text{H}_{24}\text{N}_2\text{O}_8 \cdot x\text{H}_2\text{O}$, $\geq 98.0\%$), potassium iodide (KI, ACS reagent, $\geq 99.0\%$), ammonium molybdate ($(\text{NH}_4)_2\text{MoO}_4$, 99.98% trace metals basis), and sodium hydroxide (NaOH, ACS reagent, $\geq 97.0\%$) were purchased from Sigma-Aldrich (St. Louis, MO). Ethanol and N-methyl-2-pyrrolidone (NMP, $\geq 99.0\%$) were purchased from VWR (Singapore). Aqueous solutions were prepared with de-ionized water (DI- H_2O) from an ELGA PURELAB Option system with a resistivity $\geq 18.2 \text{ M}\Omega \cdot \text{cm}$. C-grade GNP were purchased from XG Sciences (Lansing, MI) and multi-walled C-grade CNT were purchased from NanoTechLabs (Yadkinville, NC). According to the manufacturer, the GNP have an average thickness of 2 nm and a diameter of $< 2 \mu\text{m}$, and the CNT have an average diameter of 15 nm and an average length of 100 μm .

The anodic filters were prepared by dispersing different weight ratio of GNP and CNT at a total concentration of 0.5 mg mL^{-1} into NMP, an organic solvent with surface energy similar to that of graphene,⁴³ followed by a probe sonication (100 W, LABSONIC[®] M, Sartorius) for 15 min. Then the sonicated mixture of 20 mL GNP:CNT and NMP were vacuum filtered onto a 5- μm Millipore JMWP PTFE membrane (Billerica, MA) and sequentially washed with 100 mL of ethanol, 100 mL of 1:1 DI- H_2O :ethanol solution, and 250 mL of DI- H_2O before use. 10 mmol L^{-1} Na_2SO_4 was used as an inert electrolyte to normalize ionic strength and conductivity.

Graphene filter characterization. Electron micrographs of graphene filters were captured via a Carl Zeiss Supra55VP field emission scanning electron microscope (SEM) (Germany) and a JEOL 2100 transmission electron microscope (TEM) (Peabody, MA). ImageJ software (Bethesda, MD) was used to analyze obtained electron micrographs and the dimension was calculated from at least 100 measurements from 2 images. The specific surface area of the filters was measured with a Micromeritics ASAP 2020 surface area and porosity analyzer (Norcross, GA). Approximately 0.1 g of filter sample was placed into a glass analysis tube and dried at 120 $^\circ\text{C}$ overnight

before analysis. The electrical resistance of the filter samples were determined via a Keithley 2400-C source meter two-point probe (Cleveland, OH) over 50 measurements. X-ray photoelectron spectroscopy (XPS) was performed on a Kratos AXIS Ultra^{DL} (Kratos, UK) with monochromatic Al K α radiation (75 W, 15 kV, $h\nu=1486.71 \text{ eV}$) under high vacuum (1×10^{-9} Torr). Binding energies of XPS were calibrated relative to the C 1s (C-C bond) at 285.0 eV and data were analyzed using XPSPEAK 4.1. Water flux measurement was carried out using the same dead-end filter driven by nitrogen gas. The applied pressure ranged from 0.03 to 0.40 bar and the area exposed to the influent solution was 706 mm^2 . Water flux was obtained by measuring the collected water volume every two minutes under a certain pressure once steady-state was reached.

Graphene-based electrochemical filtration system. Filtration experiments were conducted with an electrochemically modified Whatman membrane filter holder, as described in a previous study.⁴⁴ A perforated titanium shim was used as a cathode, and a 47-mm diameter GNP:CNT filter was used as an anode. An insulating silicone rubber O-ring was used to separate two electrodes and seal the device. GNP:CNT filters were connected to a power supply via mechanical contact with a Ti current collector and supported on a 5.0- μm pore size PTFE membrane. After sealing the filtration casing and priming with DI- H_2O , a Masterflex L/S digital peristaltic pump (Vernon Hills, IL) was used to flow DI- H_2O through the graphene-based electrochemical membrane at a flow rate of 1.5 mL min^{-1} . Electrochemistry was driven with a CHI604E electrochemical analyzer (Austin, TX). A Shimadzu UV-1800 spectrophotometer (Japan) was used to measure the concentration of ferricyanide, tetracycline, and phenol at their maximum absorbance values (λ_{max}) of 425 nm ($\epsilon = 1000 \text{ M}^{-1} \text{ cm}^{-1}$), 355 nm ($\epsilon = 13320 \text{ M}^{-1} \text{ cm}^{-1}$), and 270 nm ($\epsilon = 1310 \text{ M}^{-1} \text{ cm}^{-1}$), respectively. Oxalate was quantified using a Shimadzu total organic carbon (TOC) analyzer (Singapore) with phosphoric acid oxidation. Five standard solutions ranging from 0-200 mg L^{-1} were prepared with $\text{C}_8\text{H}_5\text{KO}_4$ for total carbon calibration and with Na_2CO_3 for total inorganic carbon calibration. Tetracycline and its degradation by-products were evaluated with a HPLC-MS/QTOF analysis, and details of the method are provided in the SI.

Electrochemical characterization. Chronoamperometry, normal pulse voltammetry (NPV), and electrochemical impedance spectroscopy (EIS) were conducted with a CHI604E electrochemical analyzer using a three-electrode system: a GNP:CNT working electrode, an Ag/AgCl reference electrode, and a titanium counter electrode. The liquid flow in the electrochemical filtration system was kept continuously for 15 min prior to a potential step. For NPV experiments, currents were recorded at 150 s after each potential step, which was found to be sufficient for non-Faradaic currents to become negligible. EIS was performed on the GNP:CNT anode using AC impedance technique with a potential amplitude of 5 mV over a frequency range of 0.1- 10^5 Hz. The results were simulated with Nyquist and/or Bode plots. ZView software (Southern Pines, NC) was used to analyze EIS data to determine individual capacitor and resistor values. The electrochemical filter was compared with a batch system ($J = 0 \text{ mL min}^{-1}$) with EIS and chronoamperometry. The batch reactor was fabricated from a filter holder with parts of the polycarbonate structure removed and electrodes directly submerged in a beaker containing 200 mL of 0.5 mmol L^{-1}

$\text{Fe}(\text{CN})_6^{4-}$ solution and 10 mmol L^{-1} Na_2SO_4 electrolyte with continuous magnetic stirring.

pH, dissolved oxygen, and hydrogen peroxide analysis. pH and dissolved oxygen concentration were measured using a 3200M Agilent multi-parameter analyzer (Santa Clara, CA) with a P3211 probe and a D6111 probe. The concentration of H_2O_2 was measured by the KI method.⁴⁵ The iodide ion (I^-) rapidly reacted with H_2O_2 to form triiodide ions (I_3^-) that presented strong absorption at a wavelength of 352 nm ($\epsilon=26\,000\text{ M}^{-1}\text{cm}^{-1}$). The 0.2 mL sample aliquots from each experiment were mixed in a quartz cuvette containing 1.0 mL of 0.10 mol L^{-1} $\text{C}_8\text{H}_5\text{KO}_4$, and 0.75 mL of solution containing 0.4 mol L^{-1} KI, 0.06 mol L^{-1} NaOH, and 10^{-4} mol L^{-1} $(\text{NH}_4)_2\text{MoO}_4$. All absorbance values were measured at ambient temperature using a Shimadzu UV-1800 spectrophotometer.

Results and discussion

Design and characterization of GNP-CNT electrochemical filter.

The schematic of the graphene-based electrochemical filtration device is shown in Fig. 1a. To achieve high permeability, relatively low amount of GNP (10 mg) were used to prepare the graphene filter. The fabricated thin and flexible graphene-based filter on a PTFE membrane is shown in Fig. 1b. A previous study had indicated that unmodified graphene was susceptible to corrugation due to the presence of sp^3 hybridized carbon and topological defects,⁴⁶ which may provide nanochannels that are permeable to fluids.³⁴ Examination of SEM images identified corrugation of the graphene membrane (Fig. S2). Nanochannels caused by graphene corrugation, defects, and/or the voids among layers of GNP could help the influent flow through the filter system. Furthermore, the fluid may also flow through the interstitial spaces between individual GNP, as shown in Fig. S3.

To address the durability and conductivity issues, CNT were added to GNP as conductive binders⁴⁷ and GNP itself served as scaffold for pollutants adsorption (Fig. 1c). The high aspect ratio and conductive CNT increased GNP interparticle electrical connectivity and filter conductivity, intertwined to improve filter durability, and improved permeability by preventing tight packing of GNP. SEM and TEM images of GNP filters and GNP:CNT filters (GNP:CNT = 70%:30%) are shown in Fig. 2 and SEM images of other GNP-CNT filter ratio are shown in Fig. S4.

The water permeation rate increased linearly with increasing applied pressure and a flux of $2116\text{ L m}^{-2}\text{ h}^{-1}\text{ bar}^{-1}$ was obtained for pure GNP membrane (Fig. S5). Although permeability improved at relatively low GNP loading, the filter durability was poor as GNP easily flaked off the surface when perturbed (Fig. S6). The physical morphology of the GNP-CNT filter before and after 2 h continuous filtration of 0.1 mmol L^{-1} tetracycline was compared and no obvious change was observed (Fig. S7). Additionally, no peeling off of graphene membrane was observed after soaking the GNP-CNT filter into DI water for one month (Fig. S8), indicating strong combination of GNP-CNT layer to the PTFE membrane. Additionally, the sheet resistance of the GNP filters was high ($4008\pm 293\ \Omega$) due to low GNP interparticle connectivity even though GNP themselves are quite conductive ($10^7\ \text{S m}^{-1}$, provided by manufacturer). The XPS result showed that the O/C ratio of GNP particles was only 4.8% (Fig. S9), indicating a high purity of the as-prepared materials.

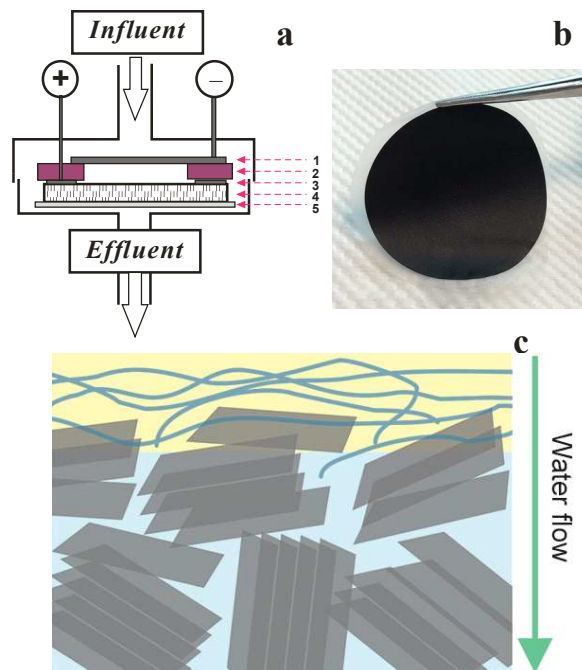


Fig. 1. (a) Schematic of an electrochemical graphene filtration system consisting of (1) a perforated titanium shim cathode, (2) an insulating silicone rubber separator and seal, (3) a titanium anodic ring, (4) a GNP:CNT anodic filter, and (5) a PTFE membrane support. (b) Image of a GNP:CNT membrane. (c) Schematic view for a GNP:CNT membrane.

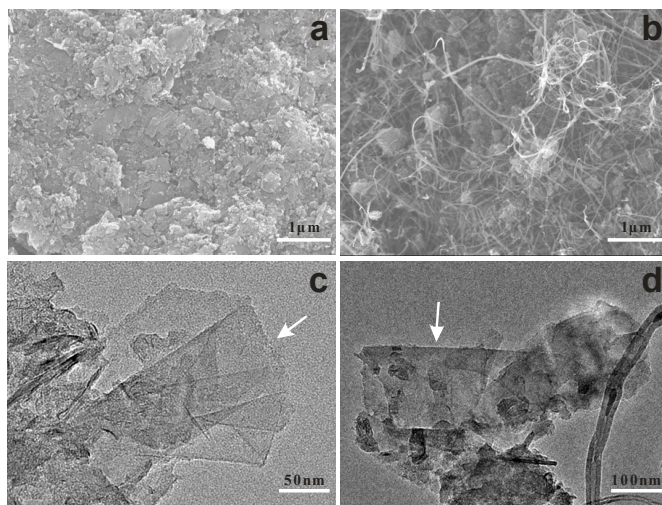


Fig. 2. SEM image of (a) GNP filters and (b) GNP:CNT filters. TEM image of (c) GNP filters and (d) GNP:CNT filters. White arrows show the monolayer (c) and multilayer (d) of GNP.

The pure GNP filters are composed of randomly oriented multilayer or monolayer GNP. The strong π - π stacking interactions between GNP and high surface energy were responsible for interparticle aggregation and stacking, which could block electron transfer sites and reduce pore size (Fig. 2a). The added CNT were intertwined with each other to serve as binders for GNP (Fig. 2b) and the GNP distributed uniformly within the CNT network. Meanwhile, the water flux increased 2.06-fold after the addition of 30% CNT (Fig. S5), which can be explained by the large pore size of CNT network that favoured water permeation. The TEM images in Fig. 2c and Fig. 2d showed the monolayer and multilayer of GNP with a

sheet shape, whose average diameter was $0.78 \pm 0.57 \mu\text{m}$ based on 100 measurements. Both GNP and GNP:CNT filters had an effective filtration area of 706 mm^2 , a similar membrane thickness of $15\text{--}20 \mu\text{m}$ (Fig. S10), and a total volume of 0.011 mL . Thus, the liquid residence time (τ) in the graphene-based filter at a flow rate of 1.5 mL min^{-1} was only 0.44 s , which is much shorter than that in a previous CNT-based filter ($\tau = 1.16 \text{ s}$).⁴⁴

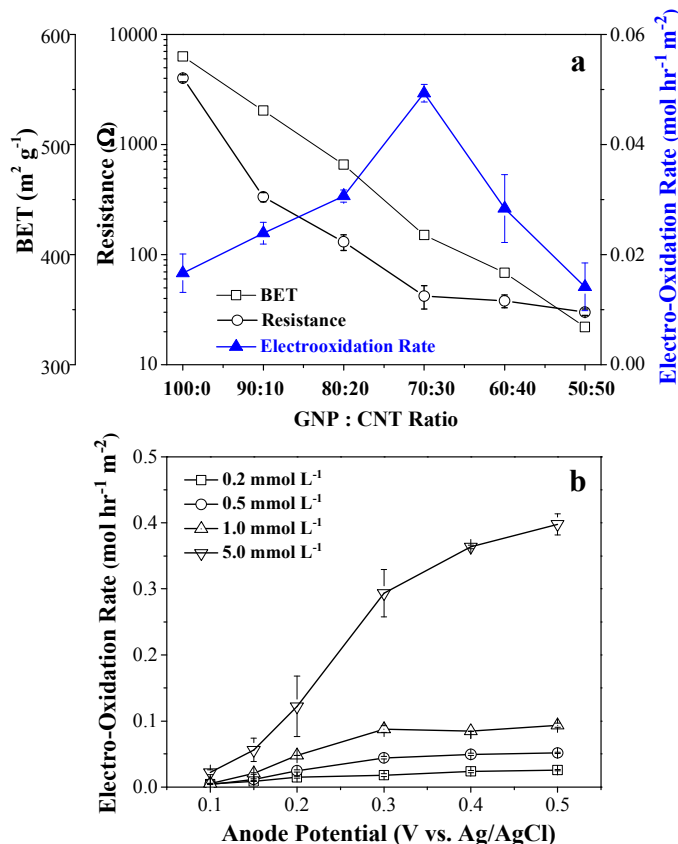


Fig. 3. Effects of GNP:CNT ratio, anode potential, and concentration on electrochemical filtration of ferrocyanide. (a) Effects of GNP:CNT ratio on electrical resistance, BET and electrooxidation rate of $0.5 \text{ mmol L}^{-1} \text{ Fe(CN)}_6^{4-}$ at anode potential of 0.4 V (vs. Ag/AgCl); (b) Concentration-dependent oxidation of Fe(CN)_6^{4-} using electrochemical graphene filter at a GNP:CNT ratio of $70\%:30\%$. Experimental conditions: Na_2SO_4 : 10 mmol L^{-1} , flow rate: 1.5 mL min^{-1} .

Effects of GNP:CNT ratio, anode potential, and influent concentration on electrochemical filtration of ferrocyanide. The GNP:CNT ratio was optimized through the measurements of electrical resistance of the filters (Fig. 3a). The electrical resistance was highest for pure GNP filter ($4008 \pm 293 \Omega$), and significantly decreased to 42 ± 10 , 38 ± 5 , and $30 \pm 2 \Omega$ with the addition of 30%, 40%, and 50% CNT, respectively. The high electrical resistance of pure GNP filters may be caused by the low electrical connectivity between neighboring GNP particles and hence more particle-particle electron hopping are needed for electron conductance. The GNP-CNT electrochemical filter was evaluated using Fe(CN)_6^{4-} as a model electron donor. The results demonstrate that the electrooxidation rate of Fe(CN)_6^{4-} increased with increasing CNT ratio from 0 to 30% (Fig. 3a) due to increasing conductivity of the filter. Further increase of CNT over 30% reduced the filter performance due to the trade-off of low specific surface area and high conductivity of CNT

(Fig. 3a). Hence, a GNP:CNT ratio of $70\%:30\%$ was identified as the optimal ratio and used for all subsequent experiments.

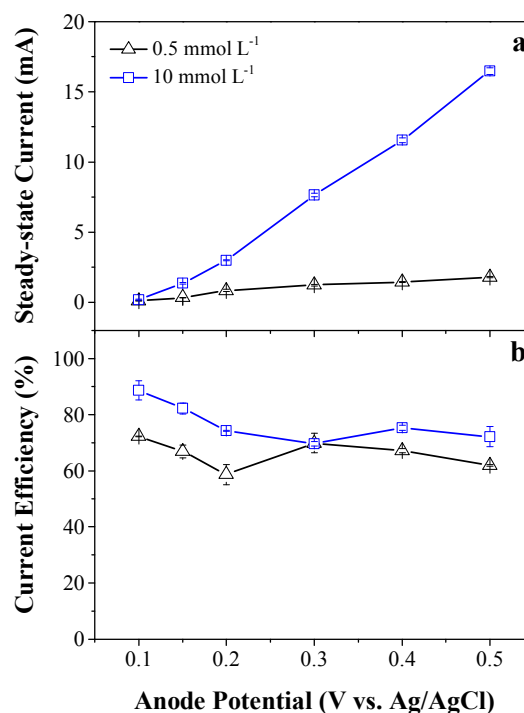
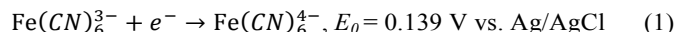


Fig. 4. Effects of influent Fe(CN)_6^{4-} concentration and anode potential on (a) steady-state current and (b) current efficiency. Experimental conditions: Na_2SO_4 : 10 mmol L^{-1} , flow rate: 1.5 mL min^{-1} , GNP:CNT= $70\%:30\%$.

The electrooxidative GNP-CNT filtration of Fe(CN)_6^{4-} was further examined as a function of anode potential and influent concentration. The electrooxidation rates for Fe(CN)_6^{4-} became non-negligible at an anode potential of 0.15 V regardless of influent concentration (Fig. 3b), indicating minimal overpotential for the oxidation reaction shown in eq. 1:



As anode potential increased above 0.15 V ($> 0.139 \text{ V}$), the electrooxidation rates for all influent concentration increased linearly up to 0.3 V (vs. Ag/AgCl). Except for $[\text{Fe(CN)}_6^{4-}]_{\text{in}} = 5.0 \text{ mmol L}^{-1}$, voltage-independent plateaus were achieved above 0.3 V (vs. Ag/AgCl), which indicated mass transport limitations. At $5 \text{ mmol L}^{-1} \text{ Fe(CN)}_6^{4-}$, increase in the electrooxidation rate started to level-off at anode potential above 0.3 V , but was never completely mass transport limited due to increased diffusion rates at higher influent Fe(CN)_6^{4-} concentration. At 0.4 V , the electrooxidation rates were 0.024 , 0.049 , 0.085 , and $0.364 \text{ mol h}^{-1} \text{ m}^{-2}$ for 0.2 , 0.5 , 1.0 , and $5.0 \text{ mmol L}^{-1} \text{ Fe(CN)}_6^{4-}$, respectively, and a linear correlation between electrooxidation rate and influent concentration was observed (Fig. S11, $R^2 > 0.99$). Thus, electrooxidation rates increased up to 15-fold by increasing influent concentration and internal electrode convection. As only one electron was transferred to oxidize Fe(CN)_6^{4-} to Fe(CN)_6^{3-} , the maximum electron transfer rates at applied anode potential of 0.4 V (vs. Ag/AgCl) were calculated as 2×10^{15} , 5×10^{15} , 1×10^{16} , and $4.3 \times 10^{16} \text{ e}^- \text{ s}^{-1}$ for 0.2 mmol L^{-1} , 0.5 mmol L^{-1} , 1.0 mmol L^{-1} , and $5.0 \text{ mmol L}^{-1} \text{ Fe(CN)}_6^{4-}$, respectively.

Change of electrochemical and effluent characteristics during electrochemical filtration of ferrocyanide. The effect of influent concentration (0.5 and 10 mmol L⁻¹) and anode potential (0.1 – 0.5 V) on the Fe(CN)₆⁴⁻ electrochemical filtration are displayed in Fig. 4. Steady-state current increased with increasing anode potential up to 0.5 V (vs. Ag/AgCl) and achieved a potential-independent mass transfer limited plateau for 0.5 mmol L⁻¹ Fe(CN)₆⁴⁻ when anode potential was above 0.4 V (Fig. 4a). No plateau was observed for 10 mmol L⁻¹ Fe(CN)₆⁴⁻ due to increased diffusion rates at higher concentration that overcome mass transfer limitations.

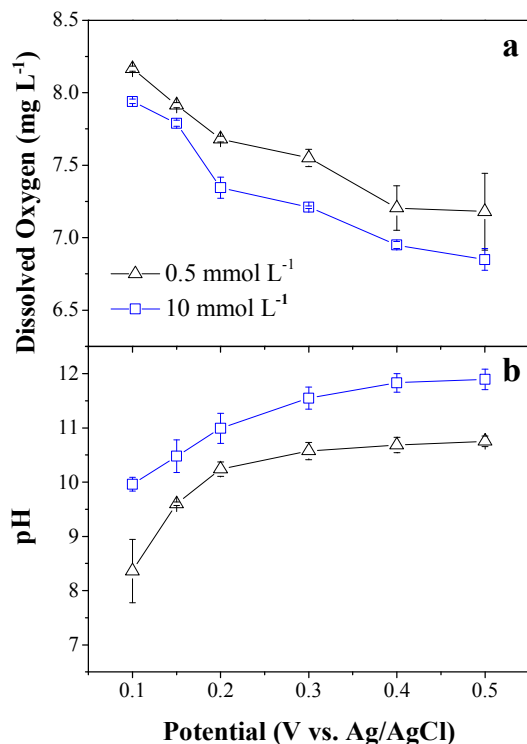
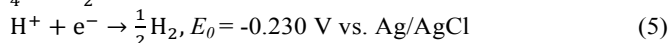
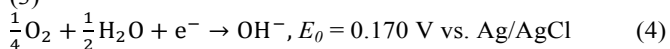
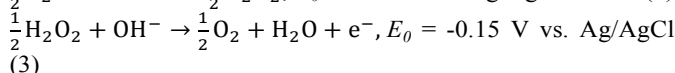
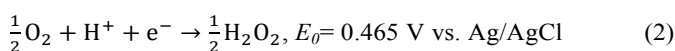


Fig. 5. Effects of influent Fe(CN)₆⁴⁻ concentration and anode potential on (a) dissolved oxygen and (b) pH. Experimental conditions: Na₂SO₄: 10 mmol L⁻¹, flow rate: 1.5 mL min⁻¹, GNP:CNT=70%:30%.

Current efficiencies fluctuated between 72% and 59% for 0.5 mmol L⁻¹ Fe(CN)₆⁴⁻ and between 89% to 72% for 10 mmol L⁻¹ Fe(CN)₆⁴⁻ (Fig. 4b). The higher current efficiency at higher concentration was due to the competitive kinetics and the fluctuations may be attributed to the production of certain reduced species (e.g., H₂O₂ production by eq. 2, pH=7) at the cathode that was subsequently oxidized at the anode (e.g. eq. 3, pH=7). This hypothesis was confirmed by continuously increased H₂O₂ concentration detected at the effluent (Fig. S12). However, the cathodic current efficiency for O₂ reduction to H₂O₂ only account for 0.7-5.5% of the overall efficiency, indicating that H₂O₂ was not the dominant reduction product. Other reactions, such as O₂ consumption (eq. 4, pH=7) and H₂ production (eq. 5, pH=7) may be the dominant cathodic reactions.



The continuously decreased concentration of dissolved oxygen further confirmed that O₂-consuming reactions happened during the electrochemical filtration processes (Fig. 5a). The levelled-off concentration of dissolved oxygen above 0.4 V were consistent with levelled-off steady-state currents above 0.4 V for 0.5 mmol L⁻¹ Fe(CN)₆⁴⁻. In this case, the O₂ molecules consumed for H₂O₂ production ranged from 0.001 to 0.007 mmol L⁻¹ (eq. 2), indicating other O₂-consuming reactions may happened simultaneously (e.g. eq. 4) by comparing the dissolved oxygen concentration in the influent and effluent. The current efficiency for eq. 4 was calculated to be 15.6-27.8% by assuming all the O₂ difference was due to eq. 4, suggesting that hydrogen production (eq. 5) could be the dominant cathodic reaction. At 10 mmol L⁻¹ Fe(CN)₆⁴⁻, the current efficiency for eq. 4 ranged from 0.25-36.9% and H⁺ was the predominant electron acceptor, which was similar to the results in 0.5 mmol L⁻¹ Fe(CN)₆⁴⁻ (Fig. S13).

pH values increased with increasing anode potential for both Fe(CN)₆⁴⁻ concentration and then levelled off at anode potential above 0.4 V (Fig. 5b), as evidenced by the change of [H⁺] (Fig. S14). Protons can be reduced at the cathode to generate hydrogen (eq. 4). This mechanism was supported by observation of visible bubbles formed on the filters (Fig. S15).

Comparison of the electrochemical GNP-CNT filter to classical batch system. The effect of internal electrode convection ($J = 0$ vs. 1.5 mL min⁻¹) on electrochemical kinetics was further examined using chronoamperometry (Fig. 6a). The initial current of the batch system (1.41 mA) decreased rapidly to a steady-state current of 0.15 mA. The initial current of the electrochemical GNP-CNT filter (27.3 mA) also decreased rapidly and then oscillated periodically around a steady-state current of 2.16 mA. Oscillations were due to periodic change in flow rate from peristaltic pump. The enhanced steady-state current for the electrochemical GNP-CNT filter (>9.4 fold) indicated that the molecular flux to the anode surface was significantly enhanced by the internal electrode convection.

The diffusion coefficient for the diffusion-limited batch system was calculated using the Cottrell equation⁴⁸:

$$I = \frac{nFAC_0\sqrt{D}}{\sqrt{\pi t}} \quad (6)$$

where I is current at time t (A), n is the number of electrons transferred, F is Faraday's constant (96,485 C mol⁻¹), A is the electrode area (cm²), C_0 is the initial target molecule concentration (mol cm⁻³), and D is the diffusion coefficient (cm² s⁻¹). The Fe(CN)₆⁴⁻ diffusion coefficient was calculated as 9.7×10^{-5} cm² s⁻¹ based on the slope of current vs. time^{-1/2} (Fig. S16), which is 13.2 times higher than the previously reported value.^{49, 50} The steady-state diffusion layer thickness ($\bar{\Delta}$) of the batch system was then calculated to be 1.7 mm using eq. 7.⁴⁸

$$\bar{\Delta} = \sqrt{2Dt} \quad (7)$$

Since the electrochemical GNP-CNT is only diffusion-limited at high anode potential, Eq. 5 and eq. 6 cannot be used to determine the diffusion layer thickness. Instead, NPV was used to provide quantitative information about mass transfer (inset Fig. 6a). At 0.4 V, the filter steady-state current (2.85 mA) was 16.2-fold higher than the batch system, in agreement with the 15-fold increase in steady-state electrooxidation kinetics from the previous section. The diffusion layer thickness electrochemical GNP-CNT filter was calculated as

105 μm , which was only 6.3% of the batch system (1.7 mm)⁵¹ and 7.0-fold greater than the GNP:CNT membrane thickness ($\sim 15 \mu\text{m}$, Fig. S10). The reduction in diffusion layer thickness was caused by hydrodynamic compression due to convective flow through the electrode.

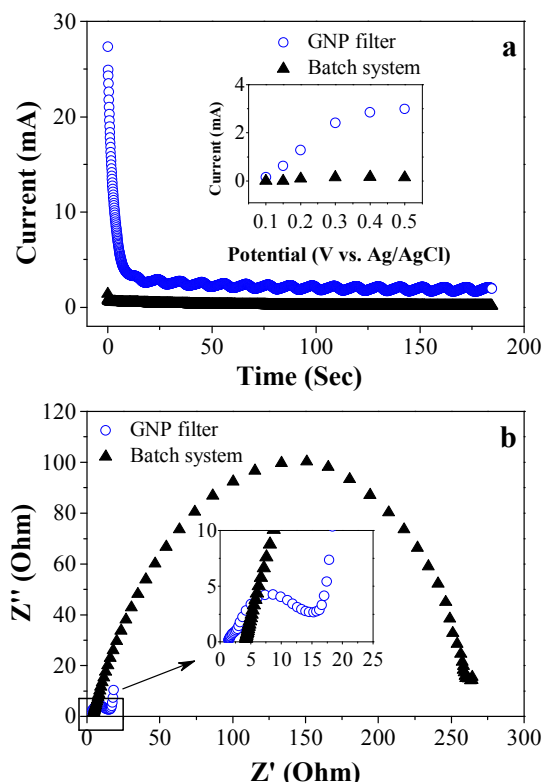


Fig. 6. Comparison of electrochemical filtration system and batch system. (a) Chronoamperometry and NPV (inset). (b) EIS and spectra magnification (inset). Experimental conditions: Na_2SO_4 : 10 mmol L^{-1} , flow rate: 1.5 mL min^{-1} , GNP:CNT=70%:30%, influent $\text{Fe}(\text{CN})_6^{4-}$: 0.5 mmol L^{-1} , anode potential: 0.4 V (vs. Ag/AgCl).

EIS for both the GNP filter and batch systems are displayed in Fig. 6b. The data were fit to a reported equivalent circuit model (Fig. S17),⁵² which had been shown to be a valid approximation for a flow-through system, to quantify the solution resistance (R_s), film resistance (R_f), charge-transfer resistance (R_{ct}), Warburg impedance, a.k.a., mass-transfer resistance (W_{mt}), film capacitance (C_f), and double-layer capacitance (CPE_{dl}) (Table S1). The GNP-CNT filter R_{ct} (12.0 Ω) and W_{mt} (4.5 Ω) were 10.8 and 7.4-fold smaller than the batch system, respectively, indicating that internal electrode convection increased target molecule mass transfer to the electrode surface and reduced mass transfer overpotential by constantly replenishing the target molecule. Based on the obtained R_{ct} value, the electron transfer rate constant (k) for $[\text{Fe}(\text{CN})_6]^{3-/4-}$ was determined with the following equation:⁵³

$$R_{CT} = \frac{RT}{n^2 F^2 A k C} \quad (8)$$

where R is the universal gas constant ($\text{J mol}^{-1} \text{K}^{-1}$), T is the absolute temperature (K), n is the number of electrons transferred, F is Faraday's constant ($96,485 \text{ C mol}^{-1}$), A is the electrode area (cm^2), and C is the molar concentration (mol). The electron transfer rate constant was calculated to be $k=6.3 \times 10^{-3} \text{ cm s}^{-1}$, in well accordance with the previously reported value of $k=6.0 \times 10^{-3} \text{ cm s}^{-1}$ for the same redox couple

occurring at an aligned CNT electrode.⁵⁴ In addition, the CPE_{dl} of the filtration system (250.0 μF) was 14-fold lower than that of the batch system, in accordance with the previous study⁵² and suggesting that the convection reduces the Debye length by inducing the rapid near electrode surface replenishment of target molecule.

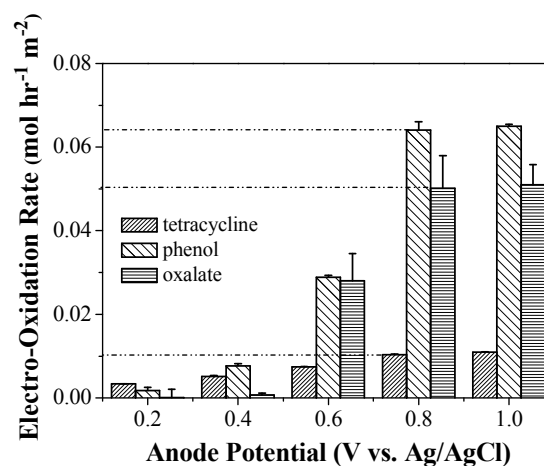
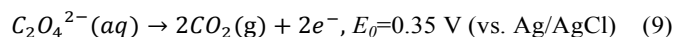


Fig. 7. Electrooxidative filtration of tetracycline, phenol and oxalate as a function of anode potential. Experimental conditions: Na_2SO_4 : 10 mmol L^{-1} , flow rate: 1.5 mL min^{-1} , GNP:CNT=70%:30%, tetracycline: 0.1 mmol L^{-1} (26 mg C L^{-1}), phenol: 0.53 mmol L^{-1} (38 mg C L^{-1}), oxalate: 0.56 mmol L^{-1} (13 mg C L^{-1}). Dashed lines represent the maximum electrooxidation rate for individual species.

Electrochemical GNP-CNT filtration of organic contaminants.

The effective and efficient removal of ferrocyanide revealed the potential of an electrochemical GNP-CNT filter for water purification. To further explore its potential for water treatment, the GNP-CNT filter was challenged with three additional organic compounds. The influent concentration of tetracycline, phenol, and oxalate were 0.1 mmol L^{-1} (26 mg C L^{-1}), 0.53 mmol L^{-1} (38 mg C L^{-1}), and 0.56 mmol L^{-1} (13 mg C L^{-1}), respectively. The complete anodic oxidation of tetracycline and phenol requires a total of 106 and 28 electrons, respectively, and only partial oxidation was expected. Oxalate requires only a 2-electron oxidation for complete mineralization to CO_2 according to eq. 9:



The control experiment using PTFE membrane alone can only physically adsorb trace organics during filtration until all sorption sites were occupied and the GNP-CNT composite anode always displayed higher electrooxidation rates than the pure GNP electrode due to a decrease in anode filter resistance (Fig. S18). The organic electrooxidation rates by GNP-CNT filters under different anode potential are shown in Fig. 7. For all three organic compounds, oxidation rates were negligible at an anode potential of 0.2 V. Electrooxidation kinetics increased with increasing anode potential until maximum removal rates of 0.010 $\text{mol hr}^{-1} \text{m}^{-2}$ (88%), 0.064 $\text{mol hr}^{-1} \text{m}^{-2}$ (93%), and 0.050 $\text{mol hr}^{-1} \text{m}^{-2}$ (87%) were achieved at 0.8 V for tetracycline, phenol, and oxalate, respectively (Fig. S18). The electrooxidation rates of phenol were 1.0 - 6.2 folds higher than those of oxalate and tetracycline due to phenol's planar aromatic structure that has strong interactions with the sp^2 -conjugated aromatic GNP-CNT sidewalls.⁵⁵

The LC-MS results showed that the characteristic tetracycline peak ($m/z = 445.16175$) was observed in the influent sample and was significantly decreased by 52.2% and 92.7% at an applied potentials of 0.6 and 0.8 V, respectively, suggesting that the parent tetracycline molecule had been mostly degraded (Figs. S19 and S20). Further increase of the applied potential over 0.8 V reduced the filter performance but also resulted in increased gas bubble formation (O_2 at anode and H_2 at cathode) that may clog filter pores, block the electroactive sites, or even degrade filter integrity. Few minor cationic products e.g. m/z of +431.1086 (peak area = 74427, 0.2% of influent tetracycline), +429.1297 (peak area = 1598305, 4.6% of influent tetracycline) and +397.1038 (peak area = 331827, 1.0% of influent tetracycline) were detected in the effluent samples, suggesting an electrooxidative bond-breaking process was active. The identification of these by-products needs further investigation.

The electrochemical degradation of pre-adsorbed tetracycline may limit the overall kinetics because of reactive site saturation by adsorbed tetracycline and/or oxidation products. Therefore, experiments were conducted with an applied cell potential prior to flowing the influent tetracycline through the electrochemical filter to evaluate the extended time electrochemical filtration performance. More than 99% of 0.1 mmol L^{-1} tetracycline was removed for the first 10 min of operation, and the removal efficiency slightly decreased and achieved an average oxidation flux of 0.011 ± 0.001 mol $hr^{-1} m^{-2}$ for the next 2 h of continuous operation. This decrement in removal efficiencies may be due to the blocked sorption sites resulted from the accumulation of tetracycline oxidation products that contributed negatively to the electrooxidation process. The lack of tetracycline breakthrough under given experimental conditions indicates that the primary removal mechanism during electrochemical filtration was oxidative degradation and no negative fouling effects on either permeability or electrochemistry were observed after 2 h. These results demonstrated a good stability of the GNP-CNT electrochemical filter.

To evaluate electrochemical filtration of phenol in real water samples, 0.53 mmol L^{-1} phenol was also spiked into a reservoir water sample (Table S2). The electrooxidation kinetics displayed a similar trend to that in DI water (Fig. S22). At an applied potential of 0.8 V vs. Ag/AgCl, the phenol spiked reservoir water oxidation flux was 0.052 ± 0.001 mol $hr^{-1} m^{-2}$, which was 18% lower than that in DI water. The natural organic matter (TOC = 4.1 mg L^{-1}), low conductivity (269 μS cm^{-1}), and relatively complex reservoir organic matrix may account for the decrement.

To further examine the extent of phenol electrooxidation, the phenol molecular flux and the relevant electron flux were compared. A 0.53 mmol L^{-1} phenol flowing at 1.5 mL min^{-1} resulted in an electron flow of 7×10^{15} molecule s^{-1} and a current of 2.7 mA at an applied anode potential of 0.8 V (vs. Ag/AgCl), which corresponds to 17×10^{16} $e^{-} s^{-1}$ (Fig. S23). Hence, a maximum of 24 electrons could be oxidized per phenol molecule, indicating partial oxidation of phenol within the filtration system. The energy consumption for electrochemical phenol filtration was calculated at a total cell potential of 2.5 V (corresponding to an anode potential of 0.8 V vs. Ag/AgCl) by assuming 24 electrons transferred per phenol molecule to be 1.9 kW hr kg^{-1} COD. Such a value is lower than state-of-the-art electrochemical oxidation processes with energy consumptions in the range of 4-100 kW hr kg^{-1} COD.^{44, 56} Additionally, the energy treated per volume was calculated to be 0.075 kW hr m^{-3} ,

which is better than other recently developed electrochemical systems at 0.1-1.0 kW hr m^{-3} ,^{57, 58} as well as other advance oxidation processes for water purification at 0.3-20 kW hr m^{-3} .^{59, 60}

Conclusions

In summary, a novel electrochemical GNP-CNT filter was developed in this study. The electrooxidation kinetics was affected by anode potential, influent concentration, target molecule properties, and anodic material. Electrochemical filtration kinetics were up to 15-fold greater than the classical batch system due to convection-enhanced transfer of the target molecule to the electrode surface and reduction of mass transfer overpotential. The effective and efficient electrooxidative filtration of ferrocyanide, tetracycline, phenol, and oxalate indicated that the novel GNP-CNT flow through filter has good potential for environmental applications. Overall, the results presented in this study quantitatively exemplified the advantages of using graphene-based electrodes in a flow-through filtration system for water purification.

Acknowledgements

This work is supported by the Singapore National Research Foundation under its Environment and Water Technologies Strategic Research Programme and administered by the Environment and Water Industry Programme Office (EWI) of the PUB on project 1102-IRIS-14-03.

Notes and references

- ^a Department of Civil and Environmental Engineering, Faculty of Engineering, National University of Singapore, 1 Engineering Drive 2, E1A-07-03, Singapore 117576
^b NUS Environmental Research Institute, National University of Singapore, 5A Engineering Drive 1, #02-01, Singapore 117411.
^c Department of Chemical and Biomolecular Engineering, National University of Singapore, Singapore 117585.
^d School of Engineering and Applied Sciences, Harvard University, Cambridge, MA, United States 02138.
^e Present address: School of Civil Engineering and Division of Environmental and Ecological Engineering, Purdue University, 550 Stadium Mall Drive, West Lafayette, Indiana, United States 47907.
^f Corresponding author: (765) 496-3559, E-mail: zhizhou@purdue.edu.
[†] Electronic Supplementary Information (ESI) available: Fig. S1-23 and Table S1-2. See DOI: 10.1039/b000000x/

- M. R. Wiesner and S. Chellam, *Environ. Sci. Technol.*, 1999, **33**, 360-366.
- M. S. Mauter and M. Elimelech, *Environ. Sci. Technol.*, 2008, **42**, 5843-5859.
- B. J. Hinds, *Curr. Opin. Solid State Mater. Sci.*, 2012, **16**, 1-9.
- X. Sun, J. Wu, Z. Chen, X. Su and B. J. Hinds, *Adv. Funct. Mater.*, 2013, **23**, 1500-1506.
- C. F. de Lannoy, D. Jassby, D. D. Davis and M. R. Wiesner, *J. Membr. Sci.*, 2012, **415-416**, 718-724.
- J. Yang, J. L. Bitter, B. A. Smith, D. H. Fairbrother and W. P. Ball, *Environ. Sci. Technol.*, 2013, **47**, 14034-14043.
- C. D. Vecitis, G. Gao and H. Liu, *J. Phys. Chem. C.*, 2011, **115**, 3621-3629.
- H. Liu, A. Vajpayee and C. D. Vecitis, *ACS Appl. Mater. Interfaces*, 2013, **5**, 10054-10066.
- B. J. Hinds, N. Chopra, T. Rantell, R. Andrews, V. Gavalas and L. G. Bachas, *Science*, 2004, **303**, 62-65.
- M. F. De Volder, S. H. Tawfick, R. H. Baughman and A. J. Hart, *Science*, 2013, **339**, 535-539.
- Y. Han, Z. Xu and C. Gao, *Adv. Funct. Mater.*, 2013, **23**, 3693-3700.

12. K. S. Novoselov, A. K. Geim, S. V. Morozov, D. Jiang, Y. Zhang, S. V. Dubonos, I. V. Grigorieva and A. A. Firsov, *Science*, 2004, **306**, 666-669.
13. M. Yoonessi, Y. Shi, D. A. Scheiman, M. Lebron-Colon, D. M. Tigelaar, R. A. Weiss and M. A. Meador, *ACS Nano*, 2012, **6**, 7644-7655.
14. S. Stankovich, D. A. Dikin, G. H. B. Dommett, K. M. Kohlhaas, E. J. Zimney, E. A. Stach, R. D. Piner, S. T. Nguyen and R. S. Ruoff, *Nature*, 2006, **442**, 282-286.
15. D. Li, M. B. Muller, S. Gilje, R. B. Kaner and G. G. Wallace, *Nat. Nanotechnol.*, 2008, **3**, 101-105.
16. M. D. Stoller, S. Park, Y. Zhu, J. An and R. S. Ruoff, *Nano Lett.*, 2008, **8**, 3498-3502.
17. M. L. Schipper, N. Nakayama-Ratchford, C. R. Davis, N. W. Kam, P. Chu, Z. Liu, X. Sun, H. Dai and S. S. Gambhir, *Nature nanotechnology*, 2008, **3**, 216-221.
18. Y. X. Xu, H. Bai, G. W. Lu, C. Li and G. Q. Shi, *J. Am. Chem. Soc.*, 2008, **130**, 5856-5857.
19. X. Wang, L. J. Zhi and K. Müllen, *Nano Lett.*, 2008, **8**, 323-327.
20. W. W. Liu, X. B. Yan, J. W. Lang, C. Peng and Q. J. Xue, *J. Mater. Chem.*, 2012, **22**, 17245-17253.
21. F. Bonaccorso, Z. Sun, T. Hasan and A. C. Ferrari, *Nat. Photonics*, 2010, **4**, 611-622.
22. X. W. Yang, L. Qiu, C. Cheng, Y. Z. Wu, Z. F. Ma and D. Li, *Angew. Chem. Int. Ed.*, 2011, **50**, 7325-7328.
23. H. Li, Z. N. Song, X. J. Zhang, Y. Huang, S. G. Li, Y. T. Mao, H. J. Ploehn, Y. Bao and M. Yu, *Science*, 2013, **342**, 95-98.
24. J. Chen, H. Bi, S. R. Sun, Y. F. Tang, W. Zhao, T. Q. Lin, D. Y. Wan, F. Q. Huang, X. D. Zhou, X. M. Xie and M. H. Jiang, *ACS Appl. Mater. Interfaces*, 2013, **5**, 1408-1413.
25. C. Chen, M. C. Long, H. D. Wu and W. M. Cai, *Sci. China Chem.*, 2012, **56**, 354-361.
26. K. Hu, M. K. Gupta, D. D. Kulkarni and V. V. Tsukruk, *Adv. Mater.*, 2013, **25**, 2301-2307.
27. K. Parvez, Z. S. Wu, R. Li, X. Liu, R. Graf, X. Feng and K. Mullen, *J Am Chem Soc*, 2014, **136**, 6083-6091.
28. K. R. Paton, E. Varrla, C. Backes, R. J. Smith, U. Khan, A. O'Neill, C. Boland, M. Lotya, O. M. Istrate, P. King, T. Higgins, S. Barwich, P. May, P. Puczkarski, I. Ahmed, M. Moebius, H. Pettersson, E. Long, J. Coelho, S. E. O'Brien, E. K. McGuire, B. M. Sanchez, G. S. Duesberg, N. McEvoy, T. J. Pennycook, C. Downing, A. Crossley, V. Nicolosi and J. N. Coleman, *Nat. Mater.*, 2014, 1-7.
29. I. Y. Jeon, Y. R. Shin, G. J. Sohn, H. J. Choi, S. Y. Bae, J. Mahmood, S. M. Jung, J. M. Seo, M. J. Kim, D. W. Chang, L. M. Dai and J. B. Baek, *Proc. Nat. Acad. Sci. USA*, 2012, **109**, 5588-5593.
30. X. H. An, T. Simmons, R. Shah, C. Wolfe, K. M. Lewis, M. Washington, S. K. Nayak, S. Talapatra and S. Kar, *Nano Lett.*, 2010, **10**, 4295-4301.
31. V. K. Gupta and T. A. Saleh, *Environ. Sci. Pollut. Res.*, 2013, **20**, 2828-2843.
32. L. Shang, T. Bian, B. H. Zhang, D. H. Zhang, L. Z. Wu, C. H. Tung, Y. D. Yin and T. R. Zhang, *Angew. Chem. Int. Ed.*, 2014, **53**, 250-254.
33. C. M. Wang, L. Ma, L. W. Liao, S. Bai, R. Long, M. Zuo and Y. J. Xiong, *Sci. Rep.*, 2013, **3**, 2580-2580.
34. G. Williams, B. Seger and P. V. Kamat, *ACS Nano*, 2008, **2**, 1487-1491.
35. E. J. Yoo, T. Okata, T. Akita, M. Kohyama, J. Nakamura and I. Honma, *Nano Lett.*, 2009, **9**, 2255-2259.
36. Y. Wang, Y. Y. Shao, D. W. Matson, J. H. Li and Y. H. Lin, *ACS Nano*, 2010, **4**, 1790-1798.
37. C. L. Su, M. Acik, K. Takai, J. Lu, S. J. Hao, Y. Zheng, P. P. Wu, Q. L. Bao, T. Enoki, Y. J. Chabal and K. P. Loh, *Nat. Commun.*, 2012, **3**, 1298-1298.
38. L. Qiu, X. H. Zhang, W. R. Yang, Y. F. Wang, G. P. Simon and D. Li, *Chem. Commun.*, 2011, **47**, 5810-5812.
39. R. A. Clark, C. J. Trout, L. E. Ritchey, A. N. Marciniak, M. Weinzierl, C. N. Schirra and D. Christopher Kurtz, *J. Electroanal. Chem.*, 2013, **689**, 284-290.
40. T. J. Kang, S. Fang, M. E. Kozlov, C. S. Haines, N. Li, Y. H. Kim, Y. Chen and R. H. Baughman, *Adv. Funct. Mater.*, 2012, **22**, 477-489.
41. C. Beriet and D. Pletcher, *J. Electroanal. Chem.*, 1993, **361**, 93-101.
42. M. H. Schnoor and C. D. Vecitis, *J. Phys. Chem. C*, 2013, **117**, 2855-2867.
43. L. Xu, J. W. McGraw, F. Gao, M. Grundy, Z. Ye, Z. Gu and J. L. Shepherd, *J. Phys. Chem. C*, 2013, **117**, 10730-10742.
44. G. D. Gao and C. D. Vecitis, *Environ. Sci. Technol.*, 2011, **45**, 9726-9734.
45. D. W. B. C. Kormann, M. R. Hoffmann, *Environ. Sci. Technol.*, 1988, **22**, 798-806.
46. K. P. Loh, Q. L. Bao, G. Eda and M. Chhowalla, *Nat. Chem.*, 2010, **2**, 1015-1024.
47. Z. Sui, Q. Meng, X. Zhang, R. Ma and B. Cao, *J. Mater. Chem.*, 2012, **22**, 8767.
48. A. J. Bard and L. R. Faulkner, *Electrochemical Methods. Fundamentals and Applications*, Wiley, New York, 2001.
49. S. J. Konopka and B. McDuffie, *Anal. Chem.*, 1970, **42**, 1741-1746.
50. S. Licht, V. Cammarata and M. S. Wrighton, *J. Phys. Chem.*, 1990, **94**, 6133-6140.
51. H. Liu and C. D. Vecitis, *J. Phys. Chem. C*, 2012, **116**, 374-383.
52. G. Gao and C. D. Vecitis, *ACS Appl. Mater. Interfaces*, 2012, **4**, 6096-6103.
53. F. Sundfors, J. Bobacka, A. Ivaska and A. Lewenstam, *Electrochim. Acta*, 2002, **47**, 2245-2251.
54. N. G. Tsierkezos and U. Ritter, *J. Chem. Thermodyn.*, 2012, **54**, 35-40.
55. B. Pan and B. Xing, *Environ. Sci. Technol.*, 2008, **42**, 9005-9013.
56. M. Panizza and G. Cerisola, *Chem. Rev.*, 2009, **109**, 6541-6569.
57. F. Ozyonar and B. Karagozoglu, *Polish J. of Environ. Stud.*, 2011, **20**, 173-179.
58. G. Zhao, P. Li, F. Nong, M. Li, J. Gao and D. Li, *J. Phys. Chem. C*, 2010, **114**, 5906-5913.
59. D. Gerrity, B. D. Stanford, R. A. Trenholm and S. A. Snyder, *Water Res.*, 2010, **44**, 493-504.
60. A. Yasar, N. Ahmad, M. N. Chaudhry, M. S. U. Rehman and A. A. Khan, *Polish J. of Environ. Stud.*, 2007, **16**, 289-294.